

# Formation of Stable Metal Halide Perovskite/Perovskite Heterojunctions

Catherine P. Clark, Jennifer E. Mann, John S. Bangsund, Wan-Ju Hsu, Eray S. Aydil, and Russell J. Holmes\*



Cite This: *ACS Energy Lett.* 2020, 5, 3443–3451



Read Online

ACCESS |



Metrics & More

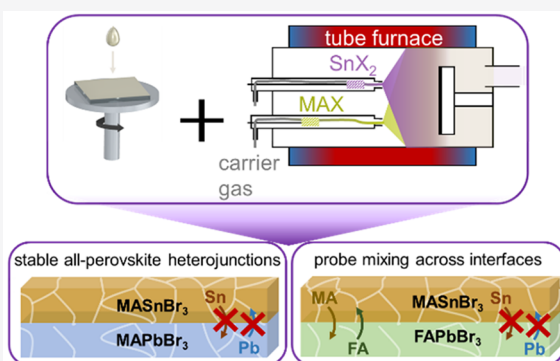


Article Recommendations



Supporting Information

**ABSTRACT:** Heterojunctions underpin the design and performance of virtually all devices based on conventional semiconductors. While metal halide perovskites have received intense attention for applications in photoconversion and optoelectronics, these devices are often hybrid, containing interfaces between the perovskite and metal oxide or organic semiconductor layers. Heterojunctions between two perovskite layers could enable new paradigms in device engineering, but to date, their formation has remained limited due to difficulty in fabricating multilayers and facile ion diffusion across interfaces. Here, sequential solution and vapor processing is used to successfully fabricate perovskite/perovskite heterojunctions comprising three-dimensional  $\text{APbX}_3/\text{CH}_3\text{NH}_3\text{SnX}_3$  [ $\text{A} = \text{CH}(\text{NH}_2)_2$ ,  $\text{CH}_3\text{NH}_3$ , or  $\text{Cs}$ ;  $\text{X} = \text{I}$  or  $\text{Br}$ ] layers. Heterojunction stability is investigated leading to the identification of two pairings that are stable for  $>1500$  h at room temperature. By probing mixing as a function of composition and grain size, we propose general design rules for the realization of stable perovskite/perovskite heterojunctions.



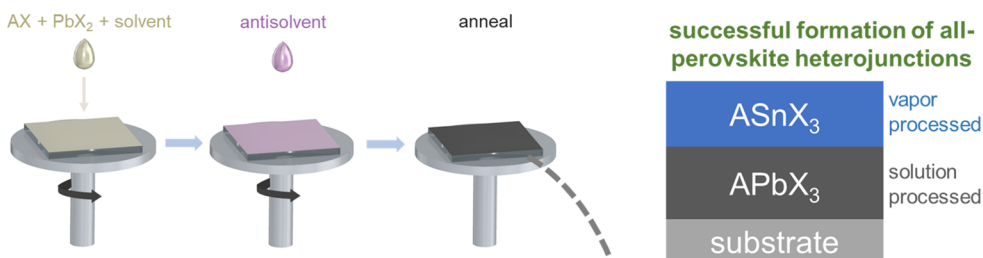
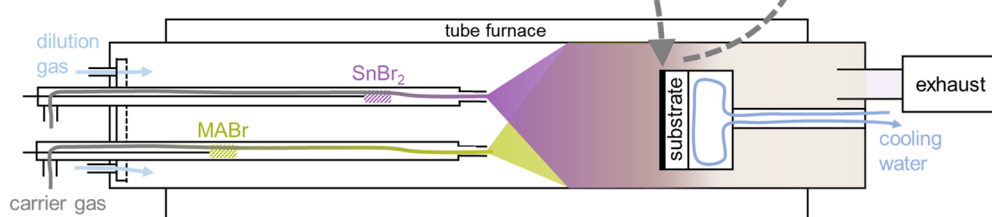
Metal halide perovskite (MHP) semiconductors show excellent promise for application in electronic and optoelectronic devices, including solar cells,<sup>1,2</sup> light-emitting devices,<sup>3</sup> lasers,<sup>4</sup> and transistors.<sup>5</sup> These devices often rely on heterojunctions between the active MHP layer and an adjacent metal oxide or organic semiconductor layer.<sup>6,7</sup> To date, the ability to effectively engineer interfaces between multiple three-dimensional (3D) MHPs has been elusive, likely due to challenges in fabricating multilayer structures using solution processing and the rapid interlayer diffusion of ionic species.<sup>8</sup> The realization of perovskite/perovskite heterojunctions would enable a broader swath of electronic and optoelectronic devices in analogy to conventional semiconductors (e.g., III–V), better utilizing the outstanding properties and tunability of MHP materials and taking advantage of their facile low-temperature processability. Stable all-perovskite heterojunctions could be used to carefully engineer band energies and charge confinement for new applications based on, for example, resonant tunneling, negative differential resistance, or quantum confinement.<sup>9,10</sup> These heterojunctions can also advance existing optoelectronic devices, for instance, by improving light absorption and energy transfer for a hole transport material-free perovskite solar cell<sup>11</sup> or by increasing the efficiency, lifetime, and photoluminescence for a green MHP light-emitting device.<sup>12</sup>

In light of their promise and broad applicability, several reports of perovskite/perovskite heterojunctions have recently emerged. However, in nearly all of these reports, at least one of the MHPs has reduced dimensionality [zero-dimensional (0D), one-dimensional (1D), and two-dimensional (2D)].<sup>13–34</sup> 1D nanowire heterostructures, for example, between  $\text{CsPbI}_3$  and  $\text{CsPbBr}_3$ , have been used to study the diffusion of halide ions and realize lateral photodetector arrays.<sup>29–31</sup> A vast majority of reported all-perovskite heterojunctions are 2D–3D or “quasi-2D” heterostructures, where a bulky organic cation separates one or more MHP layers.<sup>23,24,32,35,36</sup> 2D perovskites are typically described as  $\text{R}_2\text{A}_{n-1}\text{B}_n\text{X}_{3n+1}$ , where R is a large organic cation and  $n$  denotes the number of  $[\text{BX}_6]^{4-}$  layers separated by R cations (i.e., Ruddlesden–Popper perovskites).<sup>34</sup> Quasi-2D heterostructures have been employed to modify the energetic landscape of MHP devices.<sup>15–17</sup> Wang et al. reported the spontaneous formation of multiple quantum wells in  $\text{NMA}_2(\text{FAPbI}_3)_{n-1}\text{PbI}_4$

Received: July 26, 2020

Accepted: October 2, 2020



Scheme 1. Representation of Heterojunction Formation by Sequential Deposition of APbX<sub>3</sub> and MASnX<sub>3</sub> Perovskite Layers<sup>a</sup>Step 1: Solution Process APbX<sub>3</sub> PerovskiteStep 2: Vapor Deposit MASnX<sub>3</sub> Perovskite

<sup>a</sup>First, APbX<sub>3</sub> films are deposited via spin coating. These films are then transferred to a vapor deposition chamber where MAX and SnX<sub>2</sub> are co-deposited to form a MASnX<sub>3</sub> perovskite layer.

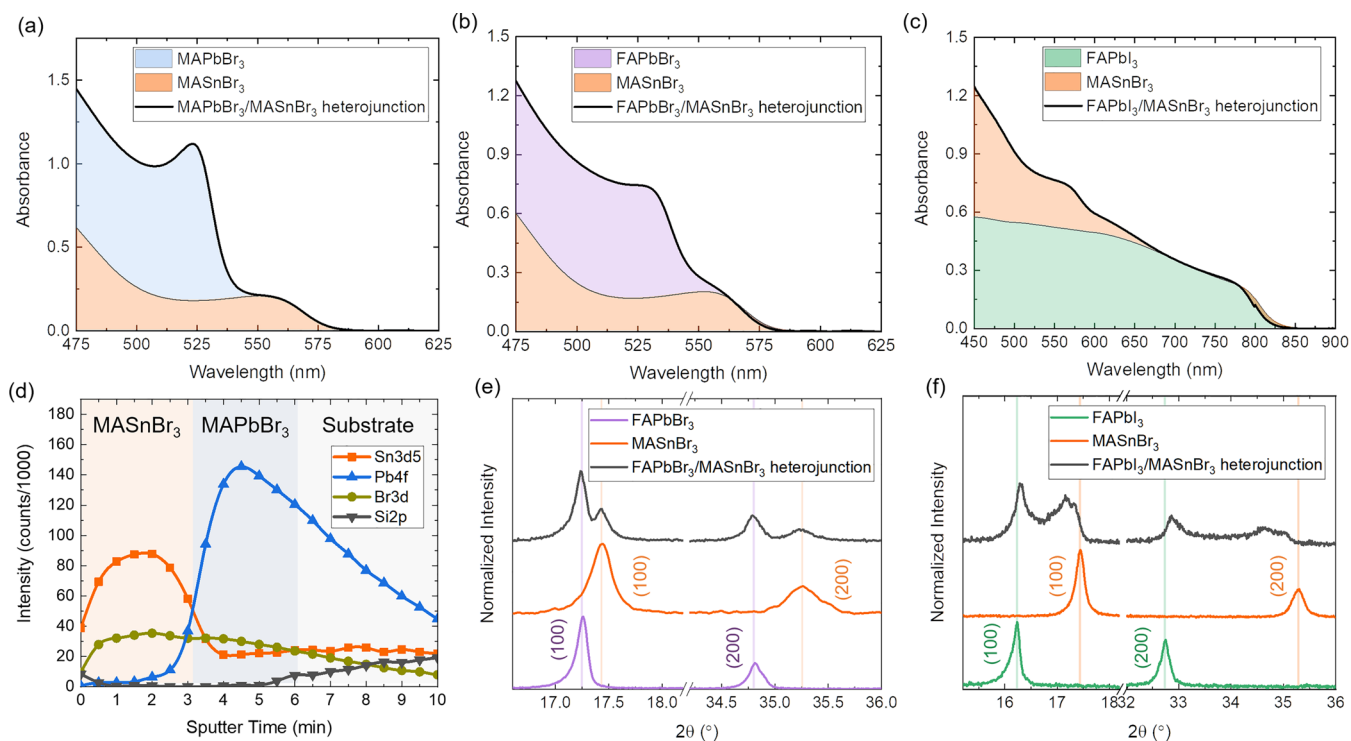


**Figure 1.** Formation of three different perovskite heterojunctions: (a and d) MAPbBr<sub>3</sub>/MASnBr<sub>3</sub>, (b and e) FAPbBr<sub>3</sub>/MASnBr<sub>3</sub>, and (c and f) FAPbI<sub>3</sub>/MASnBr<sub>3</sub>. Absorbance data (a–c) show distinct features that correspond to the absorption of the individual perovskite layers: the measured absorption of the heterojunction is very close to the superposition of the individual layer absorptions. (d) The XPS depth profile of the MAPbBr<sub>3</sub>/MASnBr<sub>3</sub> heterojunction shows a clear transition from an Sn-only MASnBr<sub>3</sub> perovskite layer to a majority Pb MAPbBr<sub>3</sub> layer; the persistence of Sn and Pb signals into the substrate is attributed to inefficient sputtering of metallic species. Shaded layers corresponding to approximate interfaces are for visualization only. XRD of (e) FAPbBr<sub>3</sub>/MASnBr<sub>3</sub> and (f) FAPbI<sub>3</sub>/MASnBr<sub>3</sub> heterojunctions shows peaks that correspond to both perovskite layers; slight peak shifts in the FAPbI<sub>3</sub>/MASnBr<sub>3</sub> heterojunction may indicate partial mixing of the two layers. XRD was performed using Co K $\alpha$  radiation, and peaks are normalized to the maximum and offset for the sake of clarity.

[NMA, 1-naphthylmethylamine; FA, formamidinium CH<sub>2</sub>(NH<sub>2</sub>)<sub>2</sub>], leading to efficient energy transfer and radiative recombination of excitons.<sup>18</sup> While promising, exclusive

reliance on self-assembled and low-dimensional structures limits the possibilities for interfacial engineering and optimization of layer properties: an example of such a

limitation in quasi-2D MHPs is the trade-off between the high stability and low charge carrier mobility due to the insulating nature of the organic R cations.<sup>37</sup> The technological importance of these structures has motivated an increasing degree of attention in the area of all-perovskite heterostructures. During the preparation of this work, Kang et al. published a 3D perovskite/perovskite heterojunction between CsPbBr<sub>3</sub> and MAPbCl<sub>3</sub> to improve the efficiency and lifetime of MHP light-emitting diodes.<sup>12</sup> This work highlights the application of this novel MHP structure to have immediate applicability in relevant optoelectronic devices. Here, we demonstrate the formation of perovskite/perovskite heterojunctions between thin films of 3D ABX<sub>3</sub> MHPs and identify two pairings with stability for >1500 h. We also identify which species are diffusing across the interface and the impact of grain size on mixing rate for a case in which multiple cations are varied across the interface. Thus, in addition to demonstrating an approach to realizing stable perovskite/perovskite heterojunctions, we offer design rules for maximizing interface stability.

To successfully form perovskite/perovskite heterojunctions, a multistep process is employed that utilizes both solution (for Pb perovskites) and vapor (for Sn perovskites) deposition methods as shown in Scheme 1 (additional details in the Supporting Information). A solution-processed layer of APbX<sub>3</sub> is deposited on glass or Si substrates followed by a layer of MASnX<sub>3</sub> deposited using a home-built carrier gas vapor deposition system described in detail elsewhere.<sup>38</sup> Briefly, starting powders of SnX<sub>2</sub> and MAX (X = Br or I) are loaded in separate sources situated inside a quartz-tube furnace. A carrier gas (N<sub>2</sub>) transports the sublimed vapors to the cooled substrate, where they condense and react to form a layer of MASnX<sub>3</sub> on top of APbX<sub>3</sub>. This multistep process circumvents the need for solvent orthogonality and/or a chemically robust interlayer for sequential solution processing, thus enabling the formation and study of all-perovskite heterojunctions with intimate contact between the MHP layers. Film thicknesses were in the range (i.e., 100–500 nm) relevant for solar cells and other optoelectronic devices and were determined from spectroscopic ellipsometry measurements by fitting the data, below the respective band gaps of the materials, using the Cauchy model.

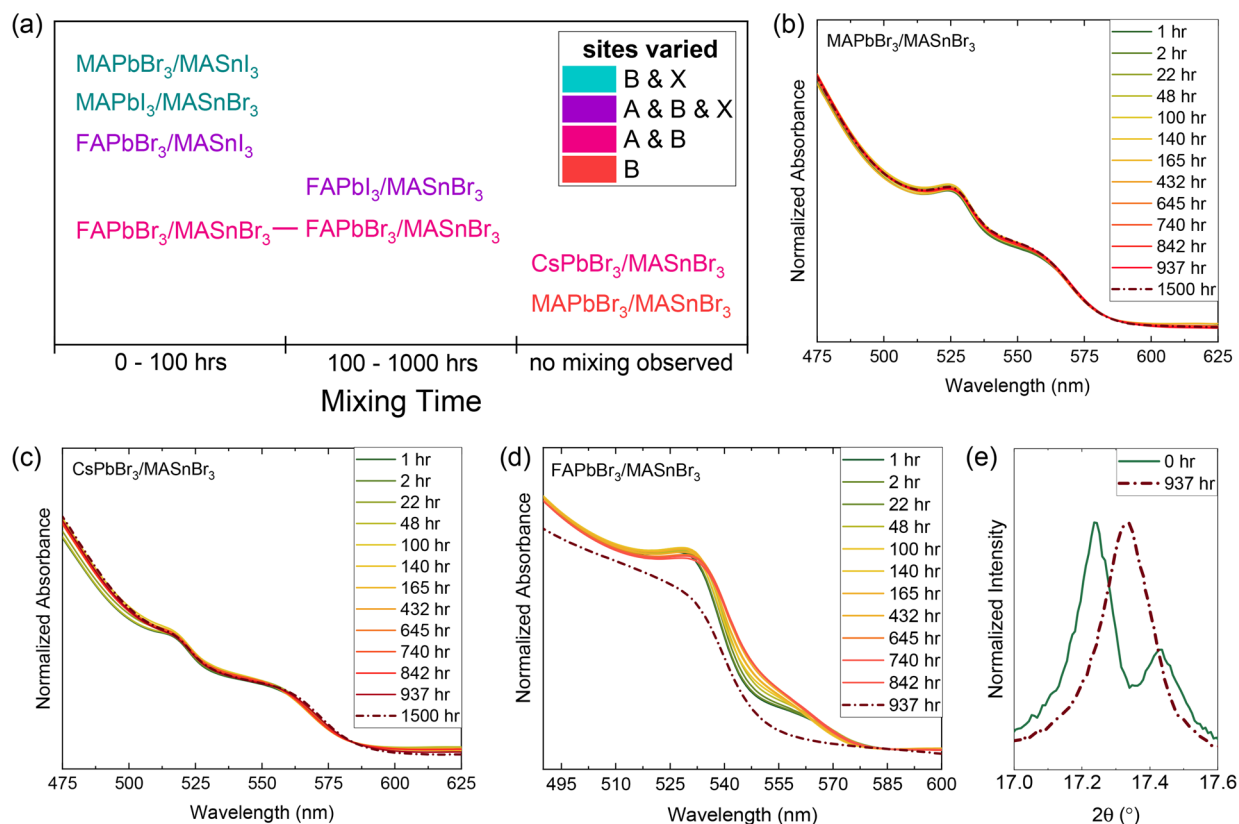
The dependence of heterojunction formation on the ions occupying the A, B, and/or X sites was examined in detail using three different structures: MAPbBr<sub>3</sub>/MASnBr<sub>3</sub> (varying only the B site), FAPbBr<sub>3</sub>/MASnBr<sub>3</sub> (varying both A and B sites), and FAPbI<sub>3</sub>/MASnBr<sub>3</sub> (varying ions on all sites). Practically, heterojunction formation is considered “successful” if the two layers remain unmixed long enough to be observed using absorption and XRD measurements, taken ~30 min and <2 h after growth, respectively.

Figure 1 shows the successful formation of MAPbBr<sub>3</sub>/MASnBr<sub>3</sub> and FAPbBr<sub>3</sub>/MASnBr<sub>3</sub> heterojunctions, and evidence of partial mixing for FAPbI<sub>3</sub>/MASnBr<sub>3</sub>. In each case, absorbance spectra show two distinct onset features that correspond to the band gaps of the constituent layers of the heterojunction. The contribution of each layer to the total absorbance is highlighted in panels a–c of Figure 1, with MASnBr<sub>3</sub> exhibiting an onset at  $\lambda \sim 580$  nm, MAPbBr<sub>3</sub> at  $\lambda \sim 540$  nm, FAPbBr<sub>3</sub> at  $\lambda \sim 550$  nm, and FAPbI<sub>3</sub> at  $\lambda \sim 825$  nm. Shading for the smaller band gap layer corresponds to the measured absorption of those individual films (MASnBr<sub>3</sub> in orange for panels a and b of Figure 1 and FAPbI<sub>3</sub> in green for

panel c of Figure 1), and shading for the larger band gap layer corresponds to the remaining absorption for the heterojunction. The total absorption of the heterojunction is nearly a superposition of the absorptions of the individual isolated films as shown in panels a–c of Figure S2. This is in contrast to the well-documented single-onset absorption spectra typical of mixed A, B, and/or X-site MHPs,<sup>39–41</sup> which would be expected if ion diffusion across the interface led to alloy formation. All absorbance spectra have backgrounds subtracted for the sake of clarity.

Heterojunction formation is also examined using X-ray photoelectron spectroscopy (XPS) sputter depth profiles or X-ray diffraction (XRD). For the MAPbBr<sub>3</sub>/MASnBr<sub>3</sub> heterojunction, the constituent layers have the same room-temperature crystal structure (*Pm*3*m*) and similar lattice parameters ( $a = 5.901$  Å for MAPbBr<sub>3</sub>, and  $a = 5.905$  Å for MASnBr<sub>3</sub>),<sup>40,42</sup> rendering their X-ray diffraction patterns indistinguishable within the diffractometer resolution limits, though the pattern is consistent with the presence of these films on the substrate as shown in Figure S2d. XPS sputter depth profiling of the MAPbBr<sub>3</sub>/MASnBr<sub>3</sub> heterojunction using a C<sub>60</sub><sup>+</sup> sputtering source (additional details in the Supporting Information) is more informative. As a function of sputter time, Figure 1d shows a transition from a high Sn 3d<sub>5/2</sub> photoelectron intensity, originating from the top MASnBr<sub>3</sub> layer (~110 nm thick), to the Pb 4f photoelectrons originating from the bottom MAPbBr<sub>3</sub> layer (~70 nm thick). After 5 min of sputtering, the Si 2p signal from the glass substrate is observed. Residual Sn and Pb counts that persist after reaching the substrate are attributed to inefficient removal of metallic species and differences in sputtering rates among organic, metallic, and halogen species, both of which have been observed in the literature.<sup>43,44</sup> While this makes it difficult to quantify interface sharpness, subsequent measurements discussed below indicate minimal diffusion for this heterojunction over thousands of hours, suggesting the overlap between Sn 3d<sub>5/2</sub> and Pb 4f photoelectron intensities in Figure 1d does not reflect B-site mixing.

For MHPs with sufficiently different lattice parameters, such as FAPbBr<sub>3</sub>/MASnBr<sub>3</sub> and FAPbI<sub>3</sub>/MASnBr<sub>3</sub>, XRD can be used to probe the crystal structure in each layer and whether the two layers have alloyed. For a heterojunction, the overall XRD pattern should contain peaks corresponding to both crystalline layers. If ion diffusion leads to substantial intermixing, an alloy would form, characterized by XRD peaks shifted from the neat materials. As shown in Figure 1e, (100) peaks corresponding to both MASnBr<sub>3</sub> ( $2\theta = 17.45^\circ$ ) and FAPbBr<sub>3</sub> ( $2\theta = 17.25^\circ$ ) are visible, confirming the formation of a FAPbBr<sub>3</sub>/MASnBr<sub>3</sub> heterojunction. An example of the absolute XRD pattern intensities is shown in Figure S3. Here, we observe that the intensities of the bottom FAPbBr<sub>3</sub> peaks are smaller in the heterojunction pattern than in the neat film due to attenuation from the top MASnBr<sub>3</sub> layer. It is interesting to note that this peak separation is less pronounced for the FAPbI<sub>3</sub>/MASnBr<sub>3</sub> heterojunction when the halogen is also varied (Figure 1f). Although the diffraction pattern for the FAPbI<sub>3</sub>/MASnBr<sub>3</sub> heterojunction shows two distinct small-angle peaks ( $2\theta = 16.31^\circ$  and  $17.25^\circ$ ), they do not align with the neat (100) FAPbI<sub>3</sub> ( $2\theta = 16.25^\circ$ ) and (100) MASnBr<sub>3</sub> peaks ( $2\theta = 17.45^\circ$ ). Moreover, there is significant diffraction intensity between the two peaks. We attribute this to mixing across the interface during the time elapsed between absorbance and XRD measurements (1–2 h). It should be



**Figure 2.** (a) Mixing times for various perovskite heterojunctions. Time-dependent absorbance of stable (b) MAPbBr<sub>3</sub>/MASnBr<sub>3</sub> and (c) CsPbBr<sub>3</sub>/MASnBr<sub>3</sub> heterojunctions, where no mixing is observed. (d) Time-dependent absorbance spectra and (e) XRD pattern for a FAPbBr<sub>3</sub>/MASnBr<sub>3</sub> heterojunction. The single absorption onset and (100) XRD peak at 937 h indicate interdiffusion of at least one species in the originally layered film. Times are rounded to the nearest hour, and all absorbance data are normalized to their value at a wavelength ( $\lambda$ ) of 585 nm for the sake of clarity. XRD was performed using Co K $\alpha$  radiation with peaks normalized to maximum.

noted that all perovskite films reported herein are in their three-dimensional  $\alpha$ -phases and have XRD patterns that are consistent with previous reports.<sup>45–50</sup> The small diffraction peak corresponding to excess PbI<sub>2</sub> (Figure S2f) observed in the neat FAPbI<sub>3</sub> film is not present in the heterojunction film; it is possible that this slight nonstoichiometry of the FAPbI<sub>3</sub> film could contribute to faster mixing by altering the defect concentration in the bottom layer.

The ability to form layered MHP structures provides a valuable method for studying the ion transport in perovskites, which is crucially related to their operation (e.g., hysteresis) and degradation. For instance, Elmelund et al. recently showed that separately fabricated films of MAPbBr<sub>3</sub> and MAPbI<sub>3</sub> placed in physical contact result in halide diffusion between these layers and are able to use this to calculate an activation energy associated with halide migration.<sup>51</sup> Our observation of mixing in structures with a variation in the halogen site is consistent with this result and first-principles calculations that reveal that the X-site species are the most mobile in the ABX<sub>3</sub> MHP lattice.<sup>52,53</sup> To probe the interfacial stability quantitatively, we examined the time evolution of seven different APbX<sub>3</sub>/MASnX<sub>3</sub> structures (Figure 2a). Here, “mixing time” is defined as the time (since deposition) at which XRD peaks corresponding to different layers merge into single peaks and/or the absorbance spectrum evolves to show a single onset feature and thus is also the time at which these data are stable and no longer change with time. Figures S5–S11 show representative XRD and absorbance data over time, while Figure 2a and Figure S12 summarize the results. The

uncertainty associated with the extracted mixing time varies between samples due to different mixing rates but is typically  $\sim 24$  h as a result of daily absorbance and XRD scans.

Interestingly, both MAPbBr<sub>3</sub>/MASnBr<sub>3</sub> and CsPbBr<sub>3</sub>/MASnBr<sub>3</sub> heterojunctions appear to be stable for >1500 h, as evinced by their unchanging absorbance spectra in panels b and c of Figure 2. MAPbBr<sub>3</sub>/MASnBr<sub>3</sub> samples heated at 60 °C for 7 h in a N<sub>2</sub> atmosphere also showed no observable mixing (Figure S13). A temperature of 60 °C was used to avoid heat-induced degradation of the individual layers while providing the means to test for the stability of the MAPbBr<sub>3</sub>/MASnBr<sub>3</sub> heterojunction, as several studies have shown that metal halide perovskites can begin to degrade at temperatures near 100 °C.<sup>54–56</sup> Varying the MASnBr<sub>3</sub> layer thickness from  $\sim 110$  to  $\sim 190$  nm also had no impact, further indicating the robustness of this interface. We also note that the stability of heterojunctions containing tin perovskites may be surprising in light of the common degradation seen among tin perovskites. Indeed, without a protective coating, vapor-deposited MASnI<sub>3</sub> films degraded slowly over hundreds to thousands of hours as has been previously reported.<sup>57,58</sup> The MASnBr<sub>3</sub> films, however, appear to be much more stable as no change in XRD patterns and absorption spectra is observed for heterostructures containing MASnBr<sub>3</sub> for more than 2 months when stored in N<sub>2</sub> (Figure 2b and Figure S11).

The mixing time of the remaining heterojunctions decreases dramatically when the halogen is varied between the layers. Some pairings, such as MAPbBr<sub>3</sub>/MASnI<sub>3</sub>, mixed so rapidly (<1 h) that characterization prior to substantial mixing is not

possible due to transfer time limitations for characterization (Figure S5). Previous studies of a fully vapor-deposited MASnI<sub>3</sub>/MASnBr<sub>3</sub> heterojunction, where only the X site was varied, showed similarly fast mixing times.<sup>38</sup> Here, we also explore mixing behavior versus layer thickness and find that we can tune the composition of MASnBr<sub>3</sub>I<sub>3-x</sub> ( $x = 0, 1.5, 2,$  or  $3$ ) perovskites by varying the layer thicknesses of MASnI<sub>3</sub> and MASnBr<sub>3</sub>.<sup>38</sup> We also find that no further annealing is necessary after vapor deposition to form phase-pure films, as we have shown previously that stoichiometric MASnX<sub>3</sub> forms across a surprisingly wide range of precursor fluxes.<sup>38</sup> Notably, despite having different halogens, the FAPbI<sub>3</sub>/MASnBr<sub>3</sub> heterostructure (Figure S8) is substantially more stable than the others. This could be due to differences in grain size and defects,<sup>59,60</sup> the impact of the A site on halogen diffusion,<sup>60,61</sup> and/or the substantially different lattice parameters of these two MHPs.<sup>40,62</sup>

Among the pairings containing a single halogen type, only FAPbBr<sub>3</sub>/MASnBr<sub>3</sub> exhibits mixing. Panels d and e of Figure 2 show that the initial  $t = 1$  h absorbance spectra (d) and XRD patterns (e) have distinct onsets and peaks, respectively, that correspond to the individual FAPbBr<sub>3</sub> ( $\sim 180$  nm thick) and MASnBr<sub>3</sub> ( $\sim 190$  nm thick) layers. Over time, these distinct onsets and peaks merge, and at 937 h, the absorbance has one clear onset and the XRD pattern has a single peak, indicating mixing. Furthermore, the location of the XRD peak ( $2\theta = 17.34^\circ$ ) after 937 h is approximately halfway between the (100) peaks of the two constituent films ( $2\theta = 17.25^\circ$  for FAPbBr<sub>3</sub>, and  $2\theta = 17.45^\circ$  for MASnBr<sub>3</sub>) as expected for a 50% FA and 50% MA composition predicted on the basis of the individual film thicknesses before mixing. The difference in absorption behavior seen in our measurements between heterojunctions that exhibit mixing, e.g., FAPbBr<sub>3</sub>/MASnBr<sub>3</sub> (Figure 2d), and those that do not exhibit any mixing, e.g., MAPbBr<sub>3</sub>/MASnBr<sub>3</sub> (Figure 2b), highlights our ability to differentiate between segregated and mixed layers using the characterization techniques presented here. The difference in stability between FAPbBr<sub>3</sub>/MASnBr<sub>3</sub> and CsPbBr<sub>3</sub>/MASnBr<sub>3</sub> heterojunctions could reflect a variety of factors, including differences in lattice parameters, bottom film morphology and defect density, and/or the impact of the A site on defect migration. In addition, this difference may also reflect the additional rotational degrees of freedom available to FA<sup>+</sup> relative to Cs<sup>+</sup>. While mechanisms of ion migration in CsPbBr<sub>3</sub> are not fully understood,<sup>63</sup> first-principles calculations suggest that the energy barriers for A-site defect migration are larger for FAPbBr<sub>3</sub> than for CsPbBr<sub>3</sub>.<sup>64</sup>

What is particularly interesting about the FAPbBr<sub>3</sub>/MASnBr<sub>3</sub> heterostructure is that both the A site (FA<sup>+</sup> and MA<sup>+</sup>) and B site (Sn<sup>2+</sup> and Pb<sup>2+</sup>) could potentially be mixing. To investigate which species are diffusing across the interface, an XPS depth profile was performed on “mixed” (measured >1500 h after deposition) and “unmixed” (measured <100 h after deposition) films (Figure 3a–d). As shown in panels a and b of Figure 3, the sharpness of the transition between Sn 3d<sub>5/2</sub> and Pb 4f photoelectron intensity profiles appears to be unchanged for the two cases, indicating minimal diffusion of the B-site cations (Sn<sup>2+</sup> and Pb<sup>2+</sup>). XPS depth profiling is particularly useful in tracking the organic A-site species in this heterojunction as the different bonding environments for MA<sup>+</sup> (C–N single bond) and FA<sup>+</sup> (C=N bond) result in resolvable differences in binding energies.<sup>65</sup> The N 1s chemical states for the unmixed case (Figure 3c) show an MA<sup>+</sup> contribution only

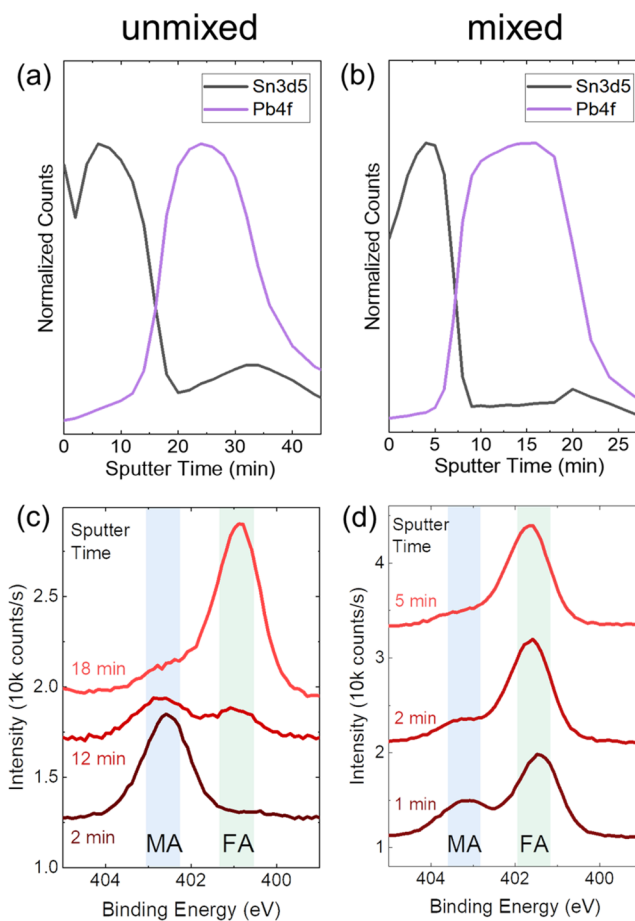


**Figure 3.** XPS depth profiles for (a and c) unmixed and (b and d) mixed FAPbBr<sub>3</sub>/MASnBr<sub>3</sub> heterojunctions, showing Sn 3d<sub>5/2</sub> and Pb 4f photoelectron intensities in panels a and b and the N 1s chemical states in panels c and d. Different sputtering time scales for the two cases reflect differences in film thicknesses. MASnBr<sub>3</sub> layers are  $\sim 110$  nm thick for the mixed case and  $\sim 190$  nm thick for the unmixed case, and FAPbBr<sub>3</sub> is fixed at  $\sim 180$  nm. Depth profiles in panels a and b are each normalized to maximum counts, and spectra in panels c and d are offset for the sake of clarity.

in the top layer of the heterojunction, whereas the mixed case (Figure 3d) has both MA<sup>+</sup> and FA<sup>+</sup> contributions throughout. The presence of the FA<sup>+</sup> species at the surface of the FAPbBr<sub>3</sub>/MASnBr<sub>3</sub> heterojunction confirms the diffusion of the A-site species from the bottom layer through the entirety of the top layer, thus suggesting that A-site diffusion is responsible for the mixing seen in panels d and e of Figure 2. The XPS spectra of all species measured are shown in Figure S14. The measurements performed herein (absorption, XRD, and XPS) could accelerate the mixing across these heterojunctions (e.g., by providing energy to diffusing species), and additional studies are needed to investigate this possibility. However, the reproducibility of mixing time between multiple heterojunction samples of the same type, e.g., 11 different MAPbBr<sub>3</sub>/MASnBr<sub>3</sub> samples (Figure S12), and the fact that we find two stable heterojunction configurations suggest that measurement artifacts are not the dominant mechanism for explaining the differences in the observed mixing times.

The diffusion of ionic species across perovskite/perovskite interfaces likely depends on several factors, including bulk and interfacial defect type and density, as well as the morphology (e.g., grain size, orientation, and roughness) and crystal

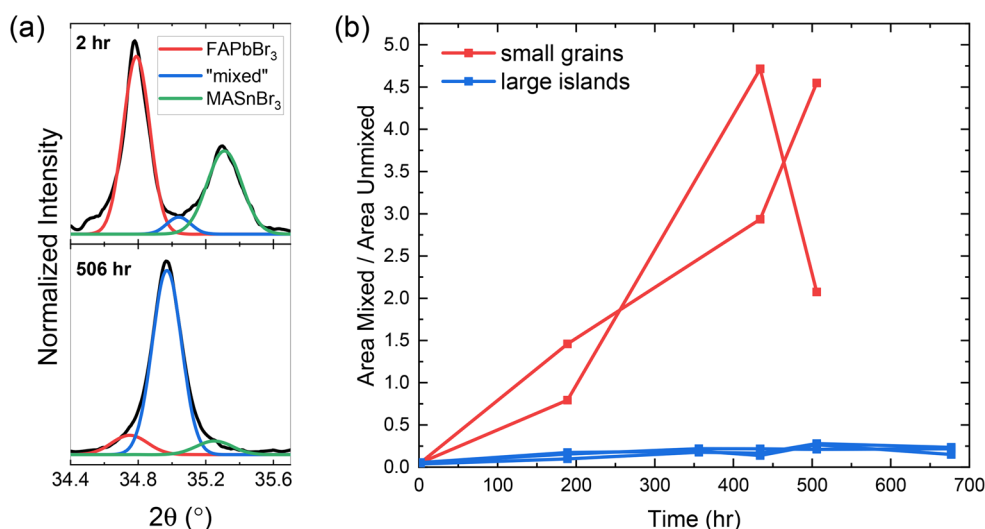


**Figure 4.** Mixing behavior of FAPbBr<sub>3</sub>/MASnBr<sub>3</sub> heterojunctions as a function of FAPbBr<sub>3</sub> grain size. (a) Example of XRD peak fitting for a small grained FAPbBr<sub>3</sub>/MASnBr<sub>3</sub> heterojunction at 2 and 506 h. XRD data were fit using three Gaussian peaks centered at  $2\theta$  values of 34.8°, 35.0°, and 35.3°. (b) Ratio of “mixed” to “unmixed” XRD peak area as a function of time. The vertical axis corresponds to the ratio of XRD peak areas corresponding to “mixed” and “unmixed” components of the film, where 0 would indicate a completely unmixed heterojunction. Heterojunctions with small grained FAPbBr<sub>3</sub> films mix at a substantially faster rate than large grained films. XRD was performed using Co K $\alpha$  radiation with peaks normalized to maximum.

structure of each layer. While ion transport may occur both in the bulk and along the grain boundaries,<sup>59,66</sup> grain boundary diffusion likely dominates in polycrystalline films.<sup>66–68</sup> To understand how much film morphology and grain size could impact diffusion, mixing times in MAPbBr<sub>3</sub>/MASnBr<sub>3</sub> and FAPbBr<sub>3</sub>/MASnBr<sub>3</sub> heterostructures were studied as a function of APbBr<sub>3</sub> (bottom film) morphology. The morphology of the APbBr<sub>3</sub> films was controlled by whether an antisolvent was used during spin coating, as described in the [Supporting Information](#). To capture extremes, two types of MAPbBr<sub>3</sub> and FAPbBr<sub>3</sub> films were fabricated, one with very small (<0.005  $\mu\text{m}^2$ ) tightly packed grains and another with very large (>3  $\mu\text{m}^2$ ) island domains (see [Figure S15](#)). While the large island domain films obtained without antisolvent may indeed contain multiple grains,<sup>69,70</sup> it is nonetheless likely that our “large island” films have larger grains than our “small grained” films, as antisolvent addition has commonly been shown to produce smaller grain sizes through increasing heterogeneous nucleation as compared to films without antisolvents.<sup>71–73</sup> The top MASnBr<sub>3</sub> layer was deposited on MAPbBr<sub>3</sub> and FAPbBr<sub>3</sub> films in a single growth to minimize morphological variations in the top layer. Despite these very different morphologies, no mixing was observed for any MAPbBr<sub>3</sub>/MASnBr<sub>3</sub> heterojunctions ([Figure S16](#)), further suggesting minimal diffusion of the B site across this interface regardless of grain boundary density.

In contrast, for FAPbBr<sub>3</sub>/MASnBr<sub>3</sub> heterostructures, the rate of mixing can be actively varied by controlling the morphology of FAPbBr<sub>3</sub>. [Figure 4](#) shows the mixing behavior of FAPbBr<sub>3</sub>/MASnBr<sub>3</sub> heterojunctions for “small grained” and “large island” FAPbBr<sub>3</sub> films over a period of 500 h. To quantify the difference in mixing rate, XRD peaks between  $2\theta$  values of 34.4° and 35.7° were fit using three Gaussian peaks corresponding to FAPbBr<sub>3</sub> ( $2\theta = 34.8^\circ$ ), MASnBr<sub>3</sub> ( $2\theta = 35.3^\circ$ ), and an alloy ( $2\theta = 35.0^\circ$ ). [Figure 4a](#) shows an example of this fitting for a “small grained” film, where the XRD pattern prior to mixing ( $t = 2$  h) can be fit primarily with peaks corresponding to FAPbBr<sub>3</sub> and MASnBr<sub>3</sub> and, after mixing ( $t =$

506 h), with a single peak corresponding to the alloy. The fit was constrained to include three peaks centered at the locations above to avoid missing small contributions from different components. For all morphologies, the X-ray beam size (>1 mm<sup>2</sup>) is several orders of magnitude larger than the domain sizes in APbBr<sub>3</sub> films. Fitting XRD patterns over time, we observe a substantial difference in the rate of mixing ([Figure 4b](#)). In [Figure 4b](#), the vertical axis is the area of the mixed (i.e., alloy) peak (at  $2\theta = 35^\circ$ ) divided by the sum of the areas of the unmixed peaks (at  $2\theta = 34.8^\circ$  and  $35.3^\circ$ ). The heterojunctions with large island FAPbBr<sub>3</sub> films show minimal mixing over 500 h, while small grained films are nearly completely mixed ([Figure S17](#)). This result supports the hypothesis that grain boundaries assist ion migration across the interface and demonstrates the dramatic impact of defect density on the stability of all-perovskite heterojunctions.

In summary, we have demonstrated the formation of all-perovskite heterojunctions between thin films of 3D ABX<sub>3</sub> MHPs. Using a combination of solution and vapor processing, we synthesize seven APbX<sub>3</sub>/MASnX<sub>3</sub> (A = Cs, MA, or FA; X = Br or I) layered structures and identify two with stability of >1500 h: MAPbBr<sub>3</sub>/MASnBr<sub>3</sub> and CsPbBr<sub>3</sub>/MASnBr<sub>3</sub>. Consistent with the literature, we find rapid mixing in structures when the halogen is different on either side of the heterojunction interface. We probe the mixing behavior of FAPbBr<sub>3</sub>/MASnBr<sub>3</sub> heterojunctions in detail and find that while A-site species diffusion is substantial over hundreds of hours, B-site diffusion is negligible. This suggests that in some cases, A-site diffusion may also lead to interface mixing, even for perovskites with the same halogen. The control of mixing rate is achieved by decreasing the grain boundary density of the bottom layer, providing insight into methods for controlling ion diffusion in MHP heterostructures. By enabling the controllable formation of a variety of 3D all-perovskite heterojunctions, this work provides a pathway to improve our understanding of ion transport in MHPs and explore the potential of all-perovskite heterostructures for advanced electronic applications.

## ■ ASSOCIATED CONTENT

### Supporting Information

The Supporting Information is available free of charge at <https://pubs.acs.org/doi/10.1021/acsenerylett.0c01609>.

Sample fabrication methods, time-dependent sample characterization to monitor heterojunction mixing, additional depth-profiled XPS spectra, SEM images, and additional fitting parameters and examples corresponding to Figure 4 (PDF)

## ■ AUTHOR INFORMATION

### Corresponding Author

Russell J. Holmes – Department of Chemical Engineering and Materials Science, University of Minnesota, Minneapolis, Minnesota 55455, United States;  [orcid.org/0000-0001-7183-3673](https://orcid.org/0000-0001-7183-3673); Email: [rholmes@umn.edu](mailto:rholmes@umn.edu)


### Authors

Catherine P. Clark – Department of Chemical Engineering and Materials Science, University of Minnesota, Minneapolis, Minnesota 55455, United States

Jennifer E. Mann – Physical Electronics, Inc., Chanhassen, Minnesota 55317, United States

John S. Bangsund – Department of Chemical Engineering and Materials Science, University of Minnesota, Minneapolis, Minnesota 55455, United States

Wan-Ju Hsu – Department of Chemical Engineering and Materials Science, University of Minnesota, Minneapolis, Minnesota 55455, United States

Eray S. Aydil – Department of Chemical and Biomolecular Engineering, Tandon School of Engineering, New York University, Brooklyn, New York 11201, United States;  [orcid.org/0000-0002-8377-9480](https://orcid.org/0000-0002-8377-9480)

Complete contact information is available at: <https://pubs.acs.org/doi/10.1021/acsenerylett.0c01609>

### Notes

The authors declare no competing financial interest.

## ■ ACKNOWLEDGMENTS

This research was funded by the National Science Foundation (NSF) through an iSuperseed grant to the University of Minnesota MRSEC (DMR-1420013), the University of Minnesota Institute on the Environment, and the University of Minnesota Industrial Partnership for Research in Interfacial and Materials Engineering (IPRIME). The authors also acknowledge support from Ronald L. and Janet A. Christenson, the 3M Science and Technology Fellowship, and the UMII MnDRIVE Graduate Assistantship. Parts of this work were carried out in the Characterization Facility, University of Minnesota, which receives partial support from NSF through the MRSEC program.

## ■ REFERENCES

- (1) Jeon, N. J.; Na, H.; Jung, E. H.; Yang, T. Y.; Lee, Y. G.; Kim, G.; Shin, H. W.; Il Seok, S.; Lee, J.; Seo, J. A Fluorene-Terminated Hole-Transporting Material for Highly Efficient and Stable Perovskite Solar Cells. *Nat. Energy* **2018**, *3*, 682–689.
- (2) Zhu, H.; Liu, Y.; Eickemeyer, F. T.; Pan, L.; Ren, D.; Ruiz-Preciado, M. A.; Carlsen, B.; Yang, B.; Dong, X.; Wang, Z.; Liu, H.; Wang, S.; Zakeeruddin, S. M.; Hagfeldt, A.; Dar, M. I.; Li, X.; Grätzel, M. Tailored Amphiphilic Molecular Mitigators for Stable Perovskite

Solar Cells with 23.5% Efficiency. *Adv. Mater.* **2020**, *32* (12), 1907757.

- (3) Lin, K.; Xing, J.; Quan, L. N.; de Arquer, F. P. G.; Gong, X.; Lu, J.; Xie, L.; Zhao, W.; Zhang, D.; Yan, C.; Li, W.; Liu, X.; Lu, Y.; Kirman, J.; Sargent, E. H.; Xiong, Q.; Wei, Z. Perovskite Light-Emitting Diodes with External Quantum Efficiency Exceeding 20%. *Nature* **2018**, *562*, 245–248.

- (4) Kim, H.; Roh, K.; Murphy, J. P.; Zhao, L.; Gunnarsson, W. B.; Longhi, E.; Barlow, S.; Marder, S. R.; Rand, B. P.; Giebink, N. C. Optically Pumped Lasing from Hybrid Perovskite Light-Emitting Diodes. *Adv. Opt. Mater.* **2020**, *8* (1), 1901297.

- (5) Yu, W.; Li, F.; Yu, L.; Niazi, M. R.; Zou, Y.; Corzo, D.; Basu, A.; Ma, C.; Dey, S.; Tietze, M. L.; Buttner, U.; Wang, X.; Wang, Z.; Hedhili, M. N.; Guo, C.; Wu, T.; Amassian, A. Single Crystal Hybrid Perovskite Field-Effect Transistors. *Nat. Commun.* **2018**, *9*, 5354.

- (6) Shin, S. S.; Lee, S. J.; Seok, S. II Metal Oxide Charge Transport Layers for Efficient and Stable Perovskite Solar Cells. *Adv. Funct. Mater.* **2019**, *29* (47), 1900455.

- (7) Said, A. A.; Xie, J.; Zhang, Q. Recent Progress in Organic Electron Transport Materials in Inverted Perovskite Solar Cells. *Small* **2019**, *15*, 1900854.

- (8) Fu, Y.; Zhu, H.; Chen, J.; Hautzinger, M. P.; Zhu, X. Y.; Jin, S. Metal Halide Perovskite Nanostructures for Optoelectronic Applications and the Study of Physical Properties. *Nat. Rev. Mater.* **2019**, *4* (3), 169–188.

- (9) Choi, W. S.; Lee, S. A.; You, J. H.; Lee, S.; Lee, H. N. Resonant Tunnelling in a Quantum Oxide Superlattice. *Nat. Commun.* **2015**, *6*, 7424.

- (10) Khan, M. E.; Lee, J.; Byeon, S.; Kim, Y. H. Semimetallicity and Negative Differential Resistance from Hybrid Halide Perovskite Nanowires. *Adv. Funct. Mater.* **2019**, *29* (13), 1807620.

- (11) Duan, Q.; Ji, J.; Hong, X.; Fu, Y.; Wang, C.; Zhou, K.; Liu, X.; Yang, H.; Wang, Z. Design of Hole-Transport-Material Free CH<sub>3</sub>NH<sub>3</sub>PbI<sub>3</sub>/CsSnI<sub>3</sub> All-Perovskite Heterojunction Efficient Solar Cells by Device Simulation. *Sol. Energy* **2020**, *201*, 555–560.

- (12) Kang, D.-H.; Kim, S.-G.; Kim, Y. C.; Han, I. T.; Jang, H. J.; Lee, J. Y.; Park, N.-G. CsPbBr<sub>3</sub>/CH<sub>3</sub>NH<sub>3</sub>PbCl<sub>3</sub> Double Layer Enhances Efficiency and Lifetime of Perovskite Light-Emitting Diodes. *ACS Energy Lett.* **2020**, *5* (7), 2191–2199.

- (13) Quan, L. N.; Quintero-Bermudez, R.; Voznyy, O.; Walters, G.; Jain, A.; Fan, J. Z.; Zheng, X.; Yang, Z.; Sargent, E. H. Highly Emissive Green Perovskite Nanocrystals in a Solid State Crystalline Matrix. *Adv. Mater.* **2017**, *29* (21), 1605945.

- (14) Li, H.; Jia, C.; Li, H.; Meng, X. CsPbX<sub>3</sub>/Cs<sub>4</sub>PbX<sub>6</sub> Core/Shell Perovskite Nanocrystals. *Chem. Commun.* **2018**, *54* (49), 6300–6303.

- (15) Proppe, A. H.; Wei, M.; Chen, B.; Quintero-Bermudez, R.; Kelley, S. O.; Sargent, E. H. Photochemically Cross-Linked Quantum Well Ligands for 2D/3D Perovskite Photovoltaics with Improved Photovoltage and Stability. *J. Am. Chem. Soc.* **2019**, *141* (36), 14180–14189.

- (16) Zhang, L.; Zhang, X.; Lu, G. Band Alignment in Two-Dimensional Halide Perovskite Heterostructures: Type I or Type II? *J. Phys. Chem. Lett.* **2020**, *11* (8), 2910–2916.

- (17) Yang, X.; Zhang, X.; Deng, J.; Chu, Z.; Jiang, Q.; Meng, J.; Wang, P.; Zhang, L.; Yin, Z.; You, J. Efficient Green Light-Emitting Diodes Based on Quasi-Two-Dimensional Composition and Phase Engineered Perovskite with Surface Passivation. *Nat. Commun.* **2018**, *9*, 570.

- (18) Wang, N.; Cheng, L.; Ge, R.; Zhang, S.; Miao, Y.; Zou, W.; Yi, C.; Sun, Y.; Cao, Y.; Yang, R.; Wei, Y.; Guo, Q.; Ke, Y.; Yu, M.; Jin, Y.; Liu, Y.; Ding, Q.; Di, D.; Yang, L.; Xing, G.; Tian, H.; Jin, C.; Gao, F.; Friend, R. H.; Wang, J.; Huang, W. Perovskite Light-Emitting Diodes Based on Solution-Processed Self-Organized Multiple Quantum Wells. *Nat. Photonics* **2016**, *10* (11), 699–704.

- (19) Ghimire, S.; Chouhan, L.; Takano, Y.; Takahashi, K.; Nakamura, T.; Yuyama, K. I.; Biju, V. Amplified and Multicolor Emission from Films and Interfacial Layers of Lead Halide Perovskite Nanocrystals. *ACS Energy Lett.* **2019**, *4* (1), 133–141.

- (20) Que, M.; Dai, Z.; Yang, H.; Zhu, H.; Zong, Y.; Que, W.; Padture, N. P.; Zhou, Y.; Chen, O. Quantum-Dot-Induced Cesium-Rich Surface Imparts Enhanced Stability to Formamidinium Lead Iodide Perovskite Solar Cells. *ACS Energy Lett.* **2019**, *4* (8), 1970–1975.
- (21) Xu, W.; He, F.; Zhang, M.; Nie, P.; Zhang, S.; Zhao, C.; Luo, R.; Li, J.; Zhang, X.; Zhao, S.; Li, W. Di.; Kang, F.; Nan, C. W.; Wei, G. Minimizing Voltage Loss in Efficient All-Inorganic CsPbI<sub>2</sub>Br Perovskite Solar Cells through Energy Level Alignment. *ACS Energy Lett.* **2019**, *4* (10), 2491–2499.
- (22) Li, F.; Zhou, S.; Yuan, J.; Qin, C.; Yang, Y.; Shi, J.; Ling, X.; Li, Y.; Ma, W. Perovskite Quantum Dot Solar Cells with 15.6% Efficiency and Improved Stability Enabled by an  $\alpha$ -CsPbI<sub>3</sub>/FAPbI<sub>3</sub> Bilayer Structure. *ACS Energy Lett.* **2019**, *4* (11), 2571–2578.
- (23) Rodríguez-Romero, J.; Sanchez-Diaz, J.; Echeverría-Arroondo, C.; Masi, S.; Esparza, D.; Barea, E. M.; Mora-Seró, I. Widening the 2D/3D Perovskite Family for Efficient and Thermal-Resistant Solar Cells by the Use of Secondary Ammonium Cations. *ACS Energy Lett.* **2020**, *5* (4), 1013–1021.
- (24) Li, C.; Pan, Y.; Hu, J.; Qiu, S.; Zhang, C.; Yang, Y.; Chen, S.; Liu, X.; Brabec, C. J.; Nazeeruddin, M. K.; Mai, Y.; Guo, F. Vertically Aligned 2D/3D Pb-Sn Perovskites with Enhanced Charge Extraction and Suppressed Phase Segregation for Efficient Printable Solar Cells. *ACS Energy Lett.* **2020**, *5* (5), 1386–1395.
- (25) Bai, F.; Zhang, J.; Yuan, Y.; Liu, H.; Li, X.; Chueh, C.; Yan, H.; Zhu, Z.; Jen, A. K. A 0D/3D Heterostructured All-Inorganic Halide Perovskite Solar Cell with High Performance and Enhanced Phase Stability. *Adv. Mater.* **2019**, *31* (48), 1904735.
- (26) Jiang, G.; Guhrenz, C.; Kirch, A.; Sonntag, L.; Bauer, C.; Fan, X.; Wang, J.; Reineke, S.; Gaponik, N.; Eychmüller, A. Highly Luminescent and Water-Resistant CsPbBr<sub>3</sub>-CsPb<sub>2</sub>Br<sub>5</sub> Perovskite Nanocrystals Coordinated with Partially Hydrolyzed Poly(Methyl Methacrylate) and Polyethylenimine. *ACS Nano* **2019**, *13* (9), 10386–10396.
- (27) Wang, B.; Zhang, C.; Huang, S.; Li, Z.; Kong, L.; Jin, L.; Wang, J.; Wu, K.; Li, L. Postsynthesis Phase Transformation for CsPbBr<sub>3</sub>/Rb<sub>4</sub>PbBr<sub>6</sub> Core/Shell Nanocrystals with Exceptional Photostability. *ACS Appl. Mater. Interfaces* **2018**, *10* (27), 23303–23310.
- (28) Yang, Y.; Dai, H.; Yang, F.; Zhang, Y.; Luo, D.; Zhang, X.; Wang, K.; Sun, X. W.; Yao, J. All-Perovskite Photodetector with Fast Response. *Nanoscale Res. Lett.* **2019**, *14*, 291.
- (29) Dou, L.; Lai, M.; Kley, C. S.; Yang, Y.; Bischak, C. G.; Zhang, D.; Eaton, S. W.; Ginsberg, N. S.; Yang, P. Spatially Resolved Multicolor CsPbX<sub>3</sub> Nanowire Heterojunctions via Anion Exchange. *Proc. Natl. Acad. Sci. U. S. A.* **2017**, *114* (28), 7216–7221.
- (30) Pan, D.; Fu, Y.; Chen, J.; Czech, K. J.; Wright, J. C.; Jin, S. Visualization and Studies of Ion-Diffusion Kinetics in Cesium Lead Bromide Perovskite Nanowires. *Nano Lett.* **2018**, *18* (3), 1807–1813.
- (31) Wang, M.; Tian, W.; Cao, F.; Wang, M.; Li, L. Flexible and Self-Powered Lateral Photodetector Based on Inorganic Perovskite CsPbI<sub>3</sub>-CsPbBr<sub>3</sub> Heterojunction Nanowire Array. *Adv. Funct. Mater.* **2020**, *30* (16), 1909771.
- (32) Krishna, A.; Gottis, S.; Nazeeruddin, M. K.; Sauvage, F. Mixed Dimensional 2D/3D Hybrid Perovskite Absorbers: The Future of Perovskite Solar Cells? *Adv. Funct. Mater.* **2019**, *29*, 1806482.
- (33) Ma, C.; Leng, C.; Ji, Y.; Wei, X.; Sun, K.; Tang, L.; Yang, J.; Luo, W.; Li, C.; Deng, Y.; Feng, S.; Shen, J.; Lu, S.; Du, C.; Shi, H. 2D/3D Perovskite Hybrids as Moisture-Tolerant and Efficient Light Absorbers for Solar Cells. *Nanoscale* **2016**, *8*, 18309.
- (34) Zhou, T.; Lai, H.; Liu, T.; Lu, D.; Wan, X.; Zhang, X.; Liu, Y.; Chen, Y. Highly Efficient and Stable Solar Cells Based on Crystalline Oriented 2D/3D Hybrid Perovskite. *Adv. Mater.* **2019**, *31* (32), 1901242.
- (35) Zhang, F.; Lu, H.; Tong, J.; Berry, J. J.; Beard, M. C.; Zhu, K. Advances in Two-Dimensional Organic-Inorganic Hybrid Perovskites. *Energy Environ. Sci.* **2020**, *13* (4), 1154–1186.
- (36) La-Placa, M.-G.; Gil-Escrig, L.; Guo, D.; Palazon, F.; Savenije, T. J.; Sessolo, M.; Bolink, H. J. Vacuum-Deposited 2D/3D Perovskite Heterojunctions. *ACS Energy Lett.* **2019**, *4*, 2893–2901.
- (37) Chen, Y.; Sun, Y.; Peng, J.; Tang, J.; Zheng, K.; Liang, Z. 2D Ruddlesden-Popper Perovskites for Optoelectronics. *Adv. Mater.* **2018**, *30*, 1703487.
- (38) Clark, C. P.; Voigt, B.; Aydil, E. S.; Holmes, R. J. Carrier-Gas Assisted Vapor Deposition for Highly Tunable Morphology of Halide Perovskite Thin Films. *Sustain. Energy Fuels* **2019**, *3* (9), 2447–2455.
- (39) Hao, F.; Stoumpos, C. C.; Chang, R. P. H.; Kanatzidis, M. G. Anomalous Band Gap Behavior in Mixed Sn and Pb Perovskites Enables Broadening of Absorption Spectrum in Solar Cells. *J. Am. Chem. Soc.* **2014**, *136* (22), 8094–8099.
- (40) Ferrara, C.; Patrini, M.; Pisanu, A.; Quadrelli, P.; Milanese, C.; Tealdi, C.; Malavasi, L. Wide Band-Gap Tuning in Sn-Based Hybrid Perovskites through Cation Replacement: The FA<sub>1-x</sub>MA<sub>x</sub>SnBr<sub>3</sub> Mixed System. *J. Mater. Chem. A* **2017**, *5* (19), 9391–9395.
- (41) McMeekin, D. P.; Sadoughi, G.; Rehman, W.; Eperon, G. E.; Saliba, M.; Horantner, M. T.; Haghighirad, A.; Sakai, N.; Korte, L.; Rech, B.; Johnston, M. B.; Herz, L. M.; Snaith, H. J. A Mixed-Cation Lead Mixed-Halide Perovskite Absorber for Tandem Solar Cells. *Science* **2016**, *351* (6269), 151–155.
- (42) Poglitsch, A.; Weber, D. Dynamic Disorder in Methylammoniumtrihalogenoplumbates (II) Observed by Millimeter-Wave Spectroscopy. *J. Chem. Phys.* **1987**, *87* (11), 6373–6378.
- (43) Noël, C.; Pescetelli, S.; Agresti, A.; Franquet, A.; Spampinato, V.; Felten, A.; di Carlo, A.; Houssiau, L.; Busby, Y. Hybrid Perovskites Depth Profiling with Variable-Size Argon Clusters and Monatomic Ions Beams. *Materials* **2019**, *12*, 726.
- (44) Hou, C.; Hung, S.; Jhang, L.; Chou, K.-J.; Hu, Y.; Chou, P.-T.; Su, W.-F.; Tsai, F.-Y.; Shieh, J.; Shyue, J.-J. Validated Analysis of Component Distribution Inside Perovskite Solar Cells and Its Utility in Unveiling Factors of Device Performance and Degradation. *ACS Appl. Mater. Interfaces* **2020**, *12* (20), 22730–22740.
- (45) Subbiah, A. S.; Agarwal, S.; Mahuli, N.; Nair, P.; van Hest, M.; Sarkar, S. K. Stable p-i-n FAPbBr<sub>3</sub> Devices with Improved Efficiency Using Sputtered ZnO as Electron Transport Layer. *Adv. Mater. Interfaces* **2017**, *4* (8), 1601143.
- (46) Arora, N.; Dar, M. I.; Abdi-Jalebi, M.; Giordano, F.; Pellet, N.; Jacopin, G.; Friend, R. H.; Zakeeruddin, S. M.; Grätzel, M. Intrinsic and Extrinsic Stability of Formamidinium Lead Bromide Perovskite Solar Cells Yielding High Photovoltage. *Nano Lett.* **2016**, *16* (11), 7155–7162.
- (47) Binek, A.; Hanusch, F. C.; Docampo, P.; Bein, T. Stabilization of the Trigonal High-Temperature Phase of Formamidinium Lead Iodide. *J. Phys. Chem. Lett.* **2015**, *6* (7), 1249–1253.
- (48) Borchert, J.; Milot, R. L.; Patel, J. B.; Davies, C. L.; Wright, A. D.; Martínez Maestro, L.; Snaith, H. J.; Herz, L. M.; Johnston, M. B. Large-Area, Highly Uniform Evaporated Formamidinium Lead Triiodide Thin Films for Solar Cells. *ACS Energy Lett.* **2017**, *2* (12), 2799–2804.
- (49) Chen, W.; Zhang, J.; Xu, G.; Xue, R.; Li, Y.; Zhou, Y.; Hou, J.; Li, Y. A Semitransparent Inorganic Perovskite Film for Overcoming Ultraviolet Light Instability of Organic Solar Cells and Achieving 14.03% Efficiency. *Adv. Mater.* **2018**, *30* (21), 1800855.
- (50) Duan, J.; Zhao, Y.; Yang, X.; Wang, Y.; He, B.; Tang, Q. Lanthanide Ions Doped CsPbBr<sub>3</sub> Halides for HTM-Free 10.14%-Efficiency Inorganic Perovskite Solar Cell with an Ultrahigh Open-Circuit Voltage of 1.594 V. *Adv. Energy Mater.* **2018**, *8* (31), 1802346.
- (51) Elmelund, T.; Scheidt, R. A.; Seger, B.; Kamat, P. V. Bidirectional Halide Ion Exchange in Paired Lead Halide Perovskite Films with Thermal Activation. *ACS Energy Lett.* **2019**, *4* (8), 1961–1969.
- (52) Eames, C.; Frost, J. M.; Barnes, P. R. F.; O'Regan, B. C.; Walsh, A.; Islam, M. S. Ionic Transport in Hybrid Lead Iodide Perovskite Solar Cells. *Nat. Commun.* **2015**, *6*, 7497.
- (53) Haruyama, J.; Sodeyama, K.; Han, L.; Tateyama, Y. First-Principles Study of Ion Diffusion in Perovskite Solar Cell Sensitizers. *J. Am. Chem. Soc.* **2015**, *137* (32), 10048–10051.
- (54) Abdelmageed, G.; Mackeen, C.; Hellier, K.; Jewell, L.; Seymour, L.; Tingwald, M.; Bridges, F.; Zhang, J. Z.; Carter, S. Effect of Temperature on Light Induced Degradation in Methyl-



ammonium Lead Iodide Perovskite Thin Films and Solar Cells. *Sol. Energy Mater. Sol. Cells* **2018**, *174*, 566–571.

(55) Juarez-Perez, E. J.; Ono, L. K.; Maeda, M.; Jiang, Y.; Hawash, Z.; Qi, Y. Photodecomposition and Thermal Decomposition in Methylammonium Halide Lead Perovskites and Inferred Design Principles to Increase Photovoltaic Device Stability. *J. Mater. Chem. A* **2018**, *6* (20), 9604–9612.

(56) Wali, Q.; Iftikhar, F. J.; Khan, M. E.; Ullah, A.; Iqbal, Y.; Jose, R. Advances in Stability of Perovskite Solar Cells. *Org. Electron.* **2020**, *78*, 105590.

(57) Jiang, X.; Wang, F.; Wei, Q.; Li, H.; Shang, Y.; Zhou, W.; Wang, C.; Cheng, P.; Chen, Q.; Chen, L.; Ning, Z. Ultra-High Open-Circuit Voltage of Tin Perovskite Solar Cells via an Electron Transporting Layer Design. *Nat. Commun.* **2020**, *11*, 1245.

(58) Liao, Y.; Liu, H.; Zhou, W.; Yang, D.; Shang, Y.; Shi, Z.; Li, B.; Jiang, X.; Zhang, L.; Quan, L. N.; Quintero-Bermudez, R.; Sutherland, B. R.; Mi, Q.; Sargent, E. H.; Ning, Z. Highly Oriented Low-Dimensional Tin Halide Perovskites with Enhanced Stability and Photovoltaic Performance. *J. Am. Chem. Soc.* **2017**, *139* (19), 6693–6699.

(59) Walsh, A.; Stranks, S. D. Taking Control of Ion Transport in Halide Perovskite Solar Cells. *ACS Energy Lett.* **2018**, *3* (8), 1983–1990.

(60) Dong, Q.; Lei, L.; Mendes, J.; So, F. Operational Stability of Perovskite Light Emitting Diodes. *J. Phys. Mater.* **2020**, *3*, 012002.

(61) Oranskaia, A.; Yin, J.; Bakr, O. M.; Brédas, J. L.; Mohammed, O. F. Halogen Migration in Hybrid Perovskites: The Organic Cation Matters. *J. Phys. Chem. Lett.* **2018**, *9* (18), 5474–5480.

(62) Fabini, D. H.; Stoumpos, C. C.; Laurita, G.; Kaltzoglou, A.; Kontos, A. G.; Falaras, P.; Kanatzidis, M. G.; Seshadri, R. Reentrant Structural and Optical Properties and Large Positive Thermal Expansion in Perovskite Formamidinium Lead Iodide. *Angew. Chem., Int. Ed.* **2016**, *55* (49), 15392–15396.

(63) Zhang, B.-B.; Wang, F.; Zhang, H.; Xiao, B.; Sun, Q.; Guo, J.; Hafsia, A. B.; Shao, A.; Xu, Y.; Zhou, J. Defect Proliferation in CsPbBr<sub>3</sub> Crystal Induced by Ion Migration. *Appl. Phys. Lett.* **2020**, *116* (6), 063505.

(64) John, R. A.; Yantara, N.; Ng, Y. F.; Narasimhan, G.; Mosconi, E.; Meggiolaro, D.; Kulkarni, M. R.; Gopalakrishnan, P. K.; Nguyen, C. A.; De Angelis, F.; Mhaisalkar, S. G.; Basu, A.; Mathews, N. Ionotropic Halide Perovskite Drift-Diffusive Synapses for Low-Power Neuromorphic Computation. *Adv. Mater.* **2018**, *30* (51), 1805454.

(65) Jacobsson, T. J.; Correa-Baena, J.-P.; Halvani Anaraki, E.; Philippe, B.; Stranks, S. D.; Bouduban, M. E. F.; Tress, W.; Schenk, K.; Teuscher, J.; Moser, J.-E.; Rensmo, H.; Hagfeldt, A. Unreacted PbI<sub>2</sub> as a Double-Edged Sword for Enhancing the Performance of Perovskite Solar Cells. *J. Am. Chem. Soc.* **2016**, *138* (32), 10331–10343.

(66) Xing, J.; Wang, Q.; Dong, Q.; Yuan, Y.; Fang, Y.; Huang, J. Ultrafast Ion Migration in Hybrid Perovskite Polycrystalline Thin Films under Light and Suppression in Single Crystals. *Phys. Chem. Chem. Phys.* **2016**, *18*, 30484–30490.

(67) Li, D.; Wu, H.; Cheng, H.; Wang, G.; Huang, Y.; Duan, X. Electronic and Ionic Transport Dynamics in Organolead Halide Perovskites. *ACS Nano* **2016**, *10*, 6933–6941.

(68) Shao, Y.; Fang, Y.; Li, T.; Wang, Q.; Dong, Q.; Deng, Y.; Yuan, Y.; Wei, H.; Wang, M.; Gruverman, A.; Shield, J.; Huang, J. Grain Boundary Dominated Ion Migration in Polycrystalline Organic-Inorganic Halide Perovskite Films. *Energy Environ. Sci.* **2016**, *9*, 1752–1759.

(69) Deng, Y.; Zheng, X.; Bai, Y.; Wang, Q.; Zhao, J.; Huang, J. Surfactant-Controlled Ink Drying Enables High-Speed Deposition of Perovskite Films for Efficient Photovoltaic Modules. *Nat. Energy* **2018**, *3* (7), 560–566.

(70) Deng, Y.; Peng, E.; Shao, Y.; Xiao, Z.; Dong, Q.; Huang, J. Scalable Fabrication of Efficient Organolead Trihalide Perovskite Solar Cells with Doctor-Bladed Active Layers. *Energy Environ. Sci.* **2015**, *8* (5), 1544–1550.

(71) Tavakoli, M. M.; Yadav, P.; Prochowicz, D.; Sponseller, M.; Osherov, A.; Bulović, V.; Kong, J. Controllable Perovskite Crystallization via Antisolvent Technique Using Chloride Additives for Highly Efficient Planar Perovskite Solar Cells. *Adv. Energy Mater.* **2019**, *9* (17), 1803587.

(72) Paek, S.; Schouwink, P.; Athanasopoulou, E. N.; Cho, K. T.; Grancini, G.; Lee, Y.; Zhang, Y.; Stellacci, F.; Nazeeruddin, M. K.; Gao, P. From Nano- to Micrometer Scale: The Role of Antisolvent Treatment on High Performance Perovskite Solar Cells. *Chem. Mater.* **2017**, *29* (8), 3490–3498.

(73) Jeon, N. J.; Noh, J. H.; Kim, Y. C.; Yang, W. S.; Ryu, S.; Seok, S., II Solvent Engineering for High-Performance Inorganic-Organic Hybrid Perovskite Solar Cells. *Nat. Mater.* **2014**, *13* (9), 897–903.